small methods
www.small-methods.com

Cathode-Electrolyte Interphase Engineering toward Fast-Charging $LiFePO_4$ Cathodes by Flash Carbon Coating

Jinhang Chen, Obinna E. Onah, Yi Cheng, Karla J. Silva, Chi Hun (Will) Choi, Weiyin Chen, Shichen Xu, Lucas Eddy, Yimo Han, Boris I. Yakobson, Yufeng Zhao, and James M. Tour**

Lithium iron phosphate ($LiFePO_4$, LFP) batteries are widely used in electric vehicles and energy storage systems due to their excellent cycling stability, affordability and safety. However, the rate performance of LFP remains limited due to its low intrinsic electronic and ionic conductivities. In this work, an ex situ flash carbon coating method is developed to enhance the interfacial properties for fast charging. A continuous, amorphous carbon layer is achieved by rapidly decomposing the precursors and depositing carbon species in a confined space within 10 s. Simultaneously, different heteroatoms can be introduced into the surface carbon matrix, which regulates the irregular growth of cathode-electrolyte interphase (CEI) and selectively facilitates the inorganic region formation. The inorganic-rich, hybrid conductive CEI not only promotes electron and ion transport but also restricts parasitic side reactions. Consequently, LFP cathodes with fluorinated carbon coatings exhibited the highest capacity of 151 mAh g^{-1} at 0.2 C and 96 mAh g^{-1} at 10 C, indicating their excellent rate capability over commercial LFP (58 mAh g^{-1} at 10 C). This solvent-free, versatile surface modification is shown for other electrode materials, providing an efficient platform for electrode-electrolyte interphase engineering through a surface post-treatment.

1. Introduction

Lithium-ion batteries (LIBs), known for their high energy density and specific energy, are the predominant technology for storing electrochemical energy in electric vehicles. Over the past decades, ternary layered oxides, including lithium nickel-manganese-cobalt oxide (NMC) and Ni-rich lithium nickel-cobalt-aluminum oxide (NCA), have been extensively studied and mass-produced due to their high energy density.[1,2] With the rising demand for electric vehicles, LIB production may face challenges due to a global shortage and geographical constraints of cobalt and nickel by 2050.[3,4] Recently, the olivine-type lithium iron phosphate (LFP) cathode garnered significant interest for its comparable reversible capacity, affordability, and superior thermal and cycling stability relative to ternary layered oxides, aligning well with future sustainable advancement of LIBs. However, LFP suffers from poor rate performance associated with low electronic conductivity (10^{-9}–10^{-10} S cm^{-1}) and low Li^+ diffusion coefficient (10^{-14} cm^2 s^{-1}).[5] Considerable effort has been dedicated to enhancing its ionic and electronic transport properties, such as downsizing LFP particles to decrease the Li^+ transport pathway,[6] partial substitution of Fe ions, which weakens the Li–O interactions and lowers the charge transfer resistance,[7,8] and conductive composite coating.[9,10] Among these approaches, carbon coating is identified as a convenient and highly effective alternative to improve electrical conductivity, mitigate metal ion dissolution, and avoid direct contact between electrolytes with the active material.[11]

In general, carbon coating on LFP is performed either in situ, where carbon precursors are mixed and calcined with iron,

J. Chen, O. E. Onah, Y. Cheng, K. J. Silva, C. H. (Will) Choi, W. Chen, S. Xu, L. Eddy, J. M. Tour
Department of Chemistry
Rice University
6100 Main Street, Houston, TX 77005, USA
E-mail: tour@rice.edu

O. E. Onah, L. Eddy
Applied Physics Program and Smalley-Curl Institute
Rice University
6100 Main Street, Houston, TX 77005, USA

The ORCID identification number(s) for the author(s) of this article can be found under https://doi.org/10.1002/smtd.202400680

DOI: 10.1002/smtd.202400680

C. H. (Will) Choi, J. M. Tour
Department of Materials Science & Nanoengineering
6100 Main Street, Houston, TX 77005, USA

Y. Han, B. I. Yakobson, J. M. Tour
Smalley-Curl Institute
Rice University
6100 Main Street, Houston, TX 77005, USA

Y. Zhao, J. M. Tour
Nanocarbon Center and the Rice Advanced Materials Institute
Rice University
6100 Main Street, Houston, TX 77005, USA
E-mail: YZhao@corban.edu

Y. Zhao
Corban University
5000 Deer Park Drive SE, Salem, Oregon 97317, USA

phosphorus, and lithium sources under a reducing atmosphere during LFP synthesis, or ex situ, in which carbon is introduced on synthesized LFP a post-treatment. While one-step in situ solid-state and wet chemical routes offer convenience, the particle size of precursors, mixing method, calcination temperature, and heating rate affect the carbon layer uniformity, thickness, and quality in conventional solid-state reactions.[12,13] Similarly, the carbon precursors, such as citric acid, glucose, and sucrose, interact with iron species in solution by chelation and, therefore, modulate the size of LFP particles in the wet chemical routes.[14–16] In comparison, the ex situ method enables the decoupling of LFP synthesis and the carbon coating process, which provides better control over each step. LFP of high crystallinity and purity can be synthesized by the molten salt method, so to take advantage of this process, an ex situ carbon coating would be useful.[17] However, to date, uniformity of an ex situ carbon coating is hard to achieve and it incurs substantial additional costs. Direct annealing of LFP with carbon sources in solid-state reactions has yielded inadequate carbon coverage on the LFP surface.[16,18] While wet chemical routes followed by calcination can produce uniform carbon coatings,[14,19,20] the introduction of solvent and extended calcination periods under a reducing atmosphere increase the cost of LFP production. Consequently, there is a demand for low-cost, efficient ex situ carbon coating techniques for LFP cathodes.

Recently, direct electrical heating has emerged as an attractive technique for materials synthesis[21–23] and modifications,[24,25] attributed to its time and energy efficiency and the ability to alter product properties through rapid kinetics and programmable conditions. Here, we demonstrate that the technique can be further extended to achieve uniform carbon coatings on LFP by adjusting the input voltage and discharge duration. The solid-state reaction is performed by decomposing precursors at ≈800 °C through fast electrical heating and depositing the carbon species onto the LFP substrate within 10 s. This method exhibited higher conversion efficiency than the gas-phase carbon coating method using acetylene and propylene gas.[26,27] Benefiting from the high heating/cooling rate, the structure of the LFP particles remains intact while the carbon sources are selectively decomposed. Heteroatoms can be introduced into the carbon matrix by varying the precursors and further promoting the CEI formation. LFP with different carbon coating layers are characterized and investigated as the cathode materials in LIBs. LFP cathodes with F-doped carbon coatings showed the highest capacity of 151 mAh g^{-1} at 0.2 C and 96 mAh g^{-1} at 10 C while maintaining over 80% capacity retention at 5 C after 500 cycles. A life cycle assessment (LCA) revealed that the FJH method reduces energy consumption and greenhouse gas (GHG) emissions by ≈90% compared to other ex situ carbon coating methods.

2. Results and Discussion

2.1. Design of the Rapid Ex Situ Carbon Coating

Before the flash Joule heating (FJH) process, LFP was mixed with carbon black (CB) and other sources (see below) in a mass ratio of 85:10:5. CB serves as the conductive medium to facilitate the electrical heating and act as the conductive additive during the cathode slurry preparation. A typical FJH process is shown in **Figure 1a**. The mixture of precursors was compressed inside a quartz tube with two graphite electrodes on each side, which were connected to the Cu electrodes and an external capacitor bank (Figures S1 and S2, Supporting Information). The safety precautions were discussed in previous work.[28] Two O-rings were installed between the Cu electrodes and the quartz tube to minimize gas leakage from the central reaction area and elevate the local pressure, which contributed to the efficient gas-phase carbon coating.[29] The reaction temperature was measured by an infrared thermometer. Within a discharging time of 500 ms, by adjusting the voltage input from 50 to 120 V, the peak temperature was tuned between 550 to 1450 °C with an ultrafast heating rate (≈10^4 °C s^{-1}) and cooling rate (≈10^3 °C s^{-1}) (Figure S3, Supporting Information). With an optimized input voltage of 70 V, the peak current passing through the sample was ≈64 A (Figure 1b), and the corresponding temperature reached ≈800 °C (Figure 1c,d). Eight other sources with low melting points were selected for heteroatom doping, some of these having been studied previously in conventional furnace reactions (Figure 1e,f). The melting points are listed for comparison since the boiling points of some precursors are uncertain. The FJH process was repeated three times (3 × 500 ms) over a 10-s-period to ensure a complete decomposition of the carbon sources. The precursors decomposed under such a temperature and released gas species within the confined quartz tube. In the FJH reaction exceeding 1200 °C (input voltage >100 V), the quartz tube is likely to explode due to the complete breakdown of PVDF and rapid gas release. The decomposition products of PVDF in the FJH process were collected and analyzed by GC-MS (Figure S4, Supporting Information). C-F species, including CF_2^+, CF_3^+, $C_2F_3^+$, and $C_2F_4^+$, were generated during the reaction and deposited on LFP particles. -C-F-, -CH-CF-, -CH_2-CF_2-, 1,3,5-trifluorobenzene are the major C-F species in the gas emissions according to previous investigation in PVDF thermal decomposition.[30,31]

Melamine is commonly used as a precursor for N-doped carbon and C_3N_4 structures through pyrolysis,[32,33] while the volatiles derived from PP,[34] PEG,[35] and PPS[36] have been thoroughly studied in previous research. These findings verify that the precursors decomposed by the FJH form volatile carbon species. Afterward, a continuous carbon coating formed on the LFP particles.

To demonstrate the advantages of FJH compared to conventional furnace treatment for carbon coating, the thermal stability of LFP is compared under several scenarios (Figure 1e). LFP experiences oxidation when annealed in air at ≈450 °C (Figure S5, Supporting Information). To obtain pure LFP, calcination is performed in an Ar/H_2 atmosphere, and the structural stability is maintained up to ≈800 °C, but prolonged heating results in LFP degradation. Iron phosphides, including FeP and Fe_2P, will be generated from the carbothermal reduction in the bulk phase, which compromises the crystallinity of LFP.[37] However, in the rapid heating and cooling rate of the FJH reaction, the structure of LFP remained unchanged while the carbon sources were selectively decomposed and deposited. Noticeable changes of LFP can be observed from X-ray diffraction (XRD) analysis at >1300 °C with an input voltage of 110 V (**Figure 2a**; Figure S3, Supporting Information). The results suggest that our rapid ex situ carbon coating method exhibits a wider operation window and better temperature modulation, which are crucial factors in coating control.

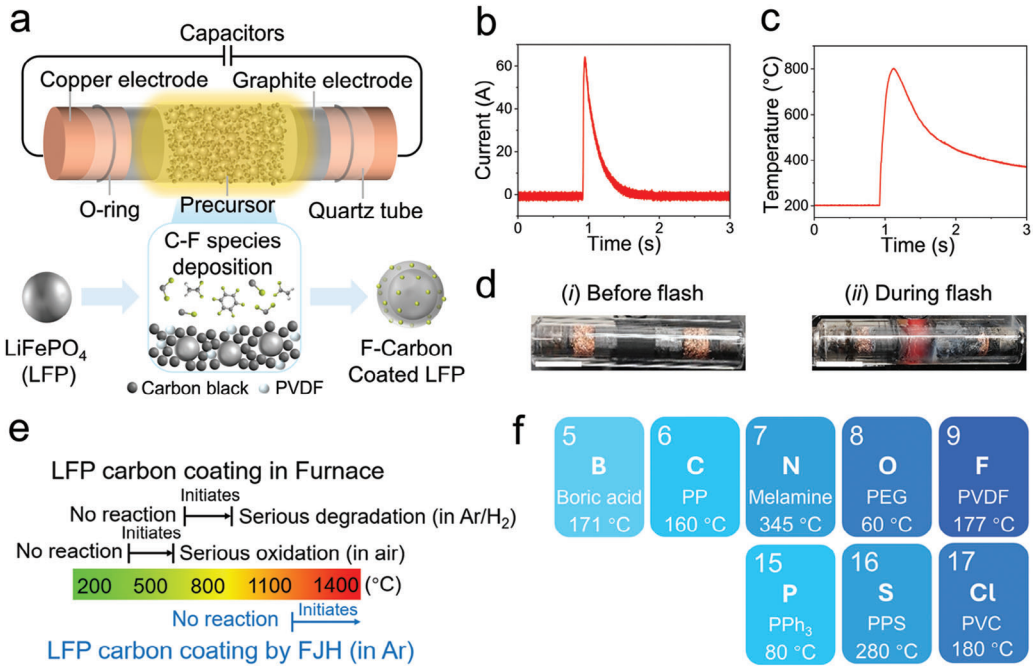

Figure 1. Ex situ carbon coating by FJH. a) Schematic diagram of the carbon coating process through gas-phase deposition in a confined space. b,c) Current curve and real-time temperature curve with an input voltage of 70 V and duration of 500 ms recorded by an infrared thermometer. d) pictures of the sample in the quartz tube i) before and ii) during the FJH reaction. Scale bar, 1 cm. e) LFP thermal stability comparison under various heating scenarios. f) Elements and corresponding precursors for heteroatom doping (melting point in note). PP: polypropylene, PEG: polyethylene glycol, PVDF: polyvinylidene fluoride, PPh_3: triphenylphosphine, PPS: polyphenylene sulfide, PVC: polyvinyl chloride.

2.2. Decomposition of Added Sources and Formation of Carbon Coating

To assess any structural change of LFP, while studying the decomposition of carbon sources in the FJH process, XRD patterns of the products were compared at different input voltages (Figure 2a). The bulk structure of LFP did not show a change between 50 and 100 V due to the short electrical heating time. However, Fe_2P formation was detected at 110 V, corresponding to a temperature of ≈1300 °C. This side reaction happens between LFP and carbon under relatively high temperatures, which is seen with reactions in conventional furnace sintering.[37] When the reaction temperature further increases to ≈1450 °C, Fe was also identified, indicating that intense reduction starts to take place. Due to the low content (5%) and low crystallinity of PVDF precursors, their diffraction peak at ≈20° is not clear. The XRD patterns of other precursors are also characterized (Figures S6 and S7, Supporting Information). The melamine and boric acid peaks disappeared after the FJH reaction at 70 V, suggesting the successful decomposition of the precursors.

The molecular vibration of the precursors can be analyzed by Fourier-transform infrared spectroscopy (FTIR). The characteristic vibrational bands of α-phase PVDF at 854, 1209, and 1423 cm^{-1} decreased after the flash at 70 V, while the intensity further diminished after the third flash (Figure 2b).[38] This intensity reduction of characteristic peaks was observed in other precursors (Figures S8–S10, Supporting Information). Thermogravimetric analysis (TGA) was conducted to further investigate the precursors decompositions. The mixture comprised 85% LFP, 10% CB, and 5% other sources (Figure 1f). LFP experienced oxidation in the air (Figure S11, Supporting Information), which caused the weight to increase at ≈430 °C. The oxidation process was not observed when annealed in an N_2 atmosphere (Figure S12, Supporting Information). CB and the other sources decompose at 500—650 °C and 200—500 °C in air, respectively, and the decomposition is complete at 800 °C with a heating rate of 10 °C/min. The TGA curves of the raw LFP-PVDF sample, after one flash at 70 V and after three flashes, are compared in Figure 2c. Since LFP and CB do not show noticeable weight loss during the rapid FJH treatment process, the difference in weight loss at 800 °C can be attributed to the content of decomposed PVDF. The PVDF content decreased from 5% to 2.8% in the first flash and 0.8% after the third flash, suggesting that most of the PVDF decomposed. High conversion ratios were also calculated from the weight loss of samples with melamine and polyphenylene sulfide (PPS) (Figures S13 and 14, Supporting Information). The surface area of the sample calculated from Brunauer-Emmett-Teller (BET) analysis decreased from 121 to 86 $m^2\ g^{-1}$ (Figure S15, Supporting Information). This is possibly due to the amorphous carbon coating deposited on the higher-surface-area carbon black, which blocks their mesoporous structure.

To characterize the oxidation state and binding environment of the heteroatom-doped LFP/C, X-ray photoelectron spectroscopy (XPS) measurements were conducted (Figure 2d–f). Semi-ionic F (≈687.6 eV) was identified in both LFP-PVDF mixtures before and after the reaction in the F 1s core-level spectra, corresponding to the C-F species in PVDF and F-doped carbon layer.[39,40] Noticeably, ionic F (≈685 eV) was present in the sample after FJH at 70 V, suggesting the possible interaction between F and Fe or Li atoms. Previous researchers have detected

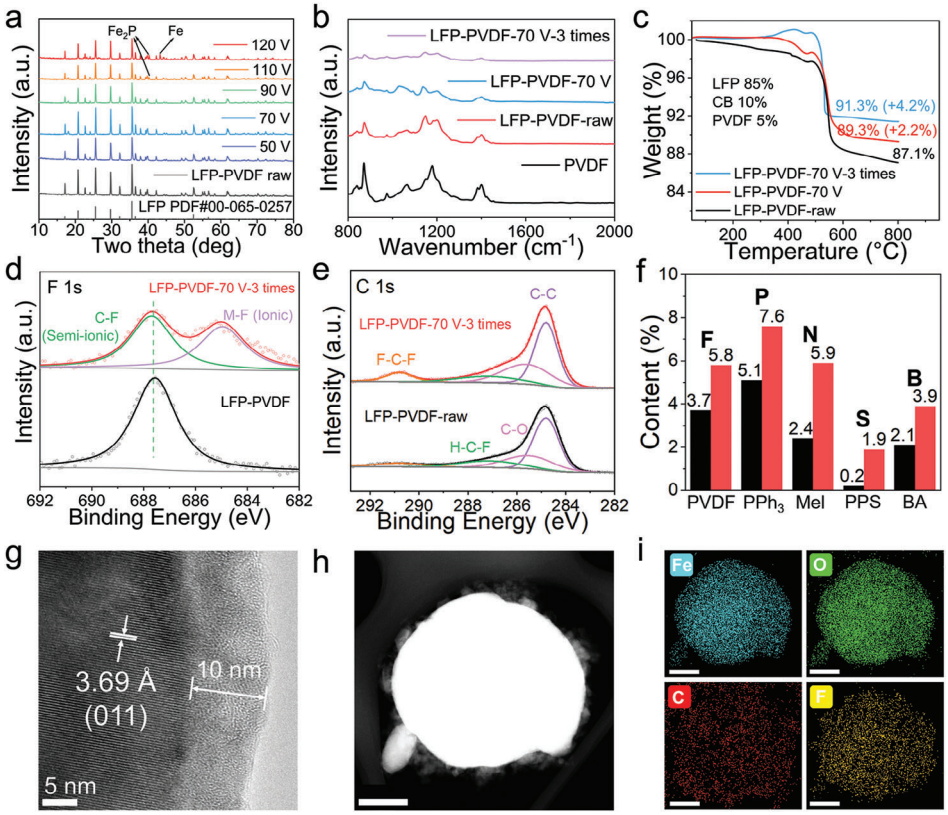

Figure 2. Characterization of precursor decomposition and carbon coating. a) XRD patterns of LFP-PVDF samples were treated under different input voltages. The PDF reference cards for each are 00-065-0257 (LFP), 04-002-3692 (Fe), and 04-006-6444 (Fe_2P). b) FTIR spectrum of LFP-PVDF samples before (red) and after FJH treatment (blue and purple). c) TGA curves of LFP-PVDF samples before (black) and after FJH treatment (red and blue) in air at the heating rate of 10 °C per min. d,e) F 1s and C 1s core-level XPS spectrum of LFP-PVDF samples before (bottom) and after FJH treatment at 70 V three times (top). f) Elemental ratios before (black) and after FJH treatment at 70 V three times (red) with different precursors. g) HRTEM image of F-LFP/C. h,i) HAADF-STEM image of F-LFP/C and corresponding elemental mapping. Scale bars, 200 nm.

the M-F species when annealing LFP with PVDF.[41] No obvious shift in peak position was observed in the O 1*s* and Fe 2*p* spectrum before and after FJH (Figure S16, Supporting Information), indicating the stability of LFP crystals during the process.[42] The two peaks at 284.8 and 285.7 eV in C 1s core-level spectra correspond to C-C and C-O bonds, respectively.[43] The flashed LFP-PVDF sample showed a higher intensity of F-C-F peak (≈290.8 eV) in the C 1s spectra. This is due to the surface enrichment effect of heteroatoms, which we also observed with other precursors (Figure 2f). Since the detection depth of XPS is ≈5–10 nm,[44] the elemental ratio determined by XPS largely reflects the surface-element distribution, hence the increases seen in Figure 1f after FJH. At elevated temperatures, carbon sources decomposed and deposited on the surface to form the carbon coating layer, together with the heteroatoms. The thickness of the carbon layer is ≈10 nm, determined by high-resolution transmission electron microscopy (HRTEM) (Figure 2g; Figure S17, Supporting Information). Only a thin amorphous layer (<2 nm) can be observed on the bare LFP surface before the FJH reaction (Figure S18, Supporting Information). High-angle annular dark-field scanning transmission electron microscopy (HAADF-STEM) images of F-doped LFP/C particles and the corresponding elemental mapping are shown in Figure 2h–i. The overlapping of Fe, O, C, and F signals confirmed the uniform coating of the entire particle. Additional elemental mappings by HAADF-STEM and scanning electron microscopy (SEM) images are provided in Figures S19 and S20 (Supporting Information). Furthermore, the carbon coating method has also been tested on other substrates, including $LiCoO_2$ (LCO), graphite, $Li_4Ti_5O_{12}$ (LTO), and $Li_{1.3}Al_{0.3}Ti_{1.7}(PO_4)_3$ (LATP). ≈10 nm carbon coating layers were observed in HRTEM images (Figure S21, Supporting Information), indicating that this flash carbon coating method has potential for testing with other electrode materials. Our ex situ post-treatment method avoids the complex interactions of precursors inherent in in situ carbon coating methods. This rapid gas-phase deposition approach exhibits low substrate dependence due to the largely reduced time scale compared to conventional furnace calcination processes. The side reactions of the electrode materials are effectively limited in the short duration while the decomposable precursors are fractured.

2.3. Battery Performance and Electrochemical Properties of Carbon Coated LFP Cathode

The electrochemical behavior of LFP cathodes is related to the input voltage. With an input voltage higher than 110 V (>1300 °C), the treated LFP cannot be charged to 3.8 V due to structure

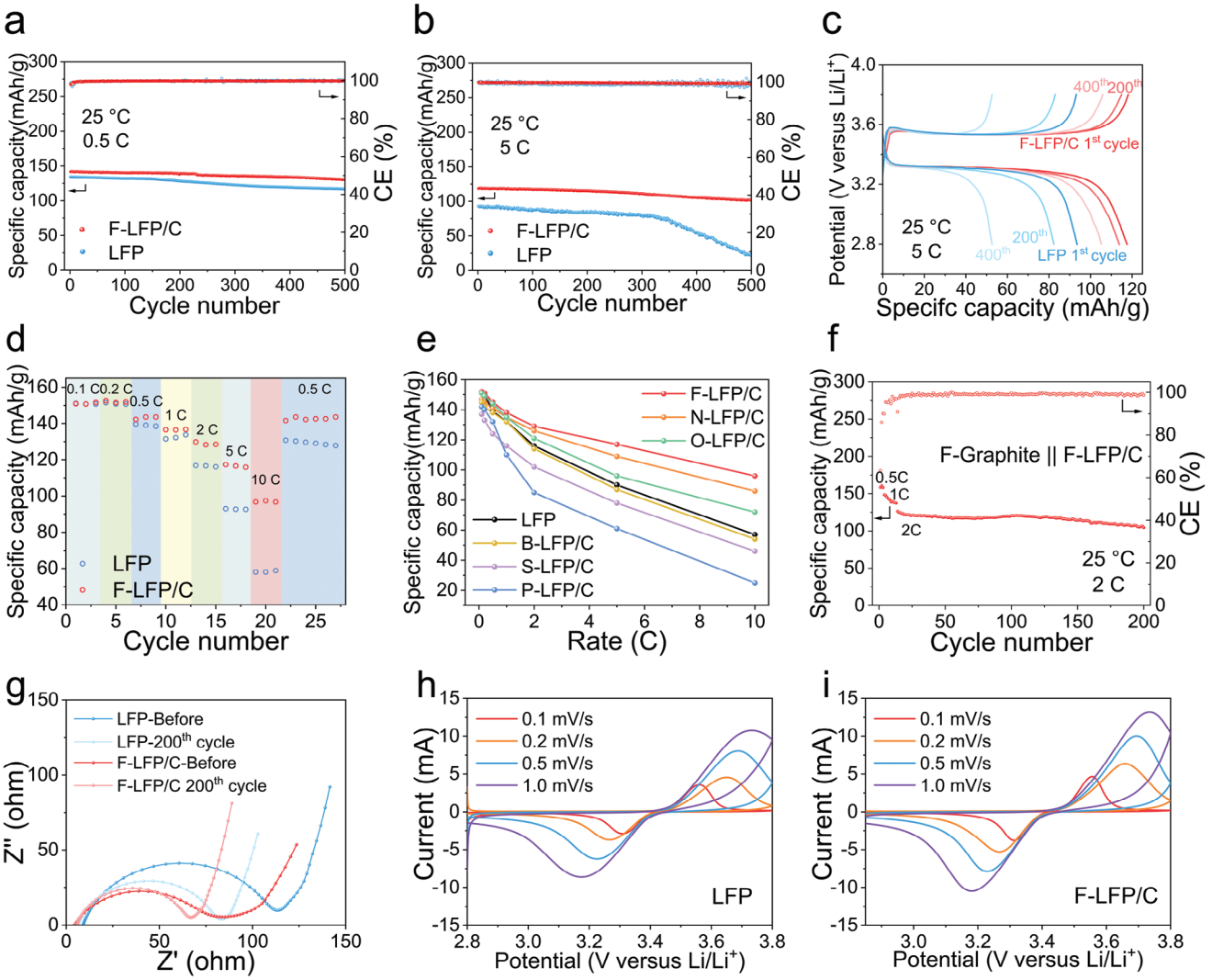

Figure 3. Electrochemical performance of F-LFP/C cathode. a,b) Cycling stability of LFP (blue) and F-LFP/C (red) at 0.5 C and 5 C, respectively. c) Charge-discharge profiles of LFP (blue) and F-LFP/C (red) at different cycles (tested at 5 C). d) Capacity of LFP (blue) and F-LFP/C (red) at different scan rates. e) Comparison of rate performance by using different carbon sources. f) Cycling stability of the full-cell LIB with F-graphite anode and F-LFP/C cathode 2 C. g) Nyquist plots of LFP (blue) and F-LFP/C (red) before and after 200 cycles. h,i) CV curves of LFP and F-LFP/C at different scan rates from 0.1 to 1 mV s^{-1}.

degradation (Figure S22, Supporting Information), which is consistent with the Fe_2P side products shown in XRD patterns (Figure 2a). The optimized condition is at 70 V (≈800 °C) three times. The F-doped carbon-coated LFP derived from PVDF (denoted as F-LFP/C) was selected as an example to investigate the electrochemical properties of LFP/C. The battery performance was analyzed in half cells where Li foil served as the counter electrode. In the galvanostatic cycling test at 0.5 C (1 C = 150 mA g^{-1}), both LFP and F-LFP/C can be reversibly charged-discharged for 500 cycles, while F-LFP/C shows slightly higher capacity retention of 92%, compared to that of 86% for pristine LFP (**Figure 3a**). The difference is more pronounced when the cathodes are tested at 5 C (Figure 3b). F-LFP/C exhibits a capacity of 118 mAh·g^{-1} and maintains 84% of the initial capacity after 500 cycles, which is higher than that of LFP (92 mAh g^{-1} and 24% retention, respectively, Figure 3c). The charging/discharging overpotentials at 5 C are higher than those at 0.5 C (Figure S23, Supporting Information). The average specific capacity of F-LFP/C is 151, 143, 137, 128, 117, and 97 mAh g^{-1} at the rate of 0.2, 0.5, C, 2, 5, and 10 C, respectively. All the values exhibit enhanced rate performance compared to bare LFP, especially a capacity increase of 67% at 10 C. By varying the PVDF content in the precursor from 2.5% to 10%, an amorphous carbon layer of 5–30 nm can be deposited with the doping of F atoms (Figures S24–S26, Supporting Information). When the PVDF content exceeds 5%, the F content only increases slightly, indicating the saturation of F atoms in the surface carbon layer during the deposition process. The highest capacity retention was observed in the 5% PVDF sample, likely due to the optimal thickness of the carbon layer (Figure S27, Supporting Information). While the carbon coating enhances the conductivity of LFP, a thick carbon layer may impede Li^+ transport. The carbon coatings derived from the various precursors are further

compared in Figure 3e (detailed in the Experimental Section). Introducing F, N, and O atoms in the carbon layers enhanced the rate performances, while S and P atoms led to a decline. In the case of B, the carbon coating, coming only from CB, was not uniform. The possible mechanism will be further discussed below.

Based on the excellent reversible capacities under a high charge/discharge rate, the F-LFP/C cathode was further tested as the cathode when paired with an F-graphite anode. The F-graphite anode was prepared by the same carbon coating process as was used in the F-LFP/C cathode. The full cell F-graphite || F-LFP/C maintained a capacity of 1.2 mAh with a retention of 85% in the initial 200 cycles (Figure 3f). The result suggests that this carbon coating process can be used on both cathodes and anodes to produce higher-rate performance systems.

The electrochemical behaviors of F-LFP/C were characterized by electrochemical impedance spectroscopy (EIS) and cyclic voltammetry (CV). The equivalent circuit used for fitting the experimental data is shown in Figures S28 and S29 (Supporting Information). The horizontal intercept in the high-frequency region is the ohmic resistance (R_o) of the electrochemical system, including the contact resistance and the resistance of active material, electrolyte, and current collectors. R_{ohm} is ≈6 ohms and remains almost unchanged during the charging and discharging process. The semicircle in the high-to-medium frequencies results from the resistance of interfacial charge transfer (R_{ct}). The sloping line at low frequency corresponds to the Warburg impedance (Z_w) related to the Li^+ diffusion.[45,46] The fitting results showed a lower R_{ct} in F-LFP/C (78 Ω) compared to LFP (108 Ω) before cycling. After 200 cycles, there is a clear enhancement of the charge transfer kinetics with the modified interphase (Figure 3g). A smaller R_{ct} decrease was observed in F-LFP/C (from 78 to 62 Ω) compared to LFP (from 108 to 77 Ω), suggesting the improved stability of the cathode electrolyte interphase (CEI).[47] CV curves of LFP and F-LFP/C were scanned at sweep rates from 0.1 – 1.0 mV s^{-1} (Figure 3h,i). The reduction peaks at 3.2 and 3.7 V are assigned to Fe^{3+} to Fe^{2+} (Li^+ insertion) and Fe^{2+} to Fe^{3+} (Li^+ extraction), respectively. The voltage gaps between the two redox peaks are ≈550 mV at 1 mV s^{-1} for LFP and F-LFP/C. Generally, Li^+ storage on electrodes includes the diffusion-controlled Faradic reaction process (typical battery materials) and surface-induced capacitive process (typically capacitor materials). The reaction kinetics through CV are examined by the following equation: $i_p = av^b$, where peak current (i_p) and the scan rates (v) obey a power law. Both a and b are adjustable parameters.[48] b values are derived from the slope of the curve of log(i_p) versus log(v) (fitting from the cathodic peak at ≈3.2 V, Figure S30, Supporting Information). The b values are close to 0.5, indicating that Li^+ diffusion is the dominant process for the LFP cathode. Furthermore, the Li^+ diffusion coefficient (D_{Li}+) is proportional to the slope of i_p versus $v^{1/2}$ according to the Randles-Sevcik equation. LFP/C cathodes, especially F-LFP/C, exhibited larger slopes than LFP (Figure S31, Supporting Information), suggesting the favorable Li^+ diffusion kinetics in LFP/C. D_{Li}+ of LFP and F-LFP/C were measured by the galvanostatic intermittent titration technique (GITT) (Figure S32 and Text S1, Supporting Information). The F-LFP/C cathode showed a higher Li^+ diffusion coefficient than the LFP cathode under different voltages, with an average increase of ≈150% (Figure S33, Supporting Information).

2.4. Formation of Inorganic-Rich Cathode-Electrolyte Interphase

The Li^+ diffusion kinetics is related to the composition of CEI, which is generally considered a heterogeneous multicomponent film formed due to electrolyte decomposition at the cathode surface.[49] The thermodynamic properties, transport kinetics, and stabilization of CEI remain less studied compared to solid-electrolyte interphase (SEI). This is due to the complex structural composition of CEI. Introducing electrolyte additives,[50,51] formation of inorganic artificial CEI,[52] and heteroatom doping of the cathode,[53] are the common strategies to tune the CEI composition. In our work, we found that introducing a heteroatom-doped carbon layer can facilitate the formation of CEI. The characterization of cycled LFP and F-LFP/C are compared in **Figure 4**. A uniform and smooth interphase morphology was observed under SEM images on F-LFP/C after cycling at 5 C rate (Figure 4d,e), while more cracks and particles were exposed at the inhomogeneous surface from LFP cathode under the same conditions (Figure 4a,b). Some large particles formed on LFP are possibly Li_2CO_3 and Li_2O (Figure S34, Supporting Information).

The morphology of CEI was further analyzed via HRTEM images. A loose, irregular, and amorphous CEI layer formed on the bare LFP cathode after cycling at 5 C rate (Figure 4c; Figure S35, Supporting Information), indicating excessive labile organic components formation due to the degradation of organic electrolyte. The loose CEI layer results in low electrical conductivity, sluggish Li^+ transfer, and poor mechanical strength. The lack of an intimate CEI layer under normal cycle conditions was reported by Zhang et al. using cryogenic electron microscopy (cryo-EM).[54] In comparison, a dense CEI layer formed in the F-LFP/C sample after cycling (Figure 4f). The CEI layer is more uniform, and Well-crystallized regions are identified in CEI, and its lattice spacing of ≈2.3 Å matches with the (111) facet of LiF.[55] The inorganic components in the CEI also constitute a much higher ratio in LFP/C with other heteroatoms and even show continuous coverage (Figure S36, Supporting Information). Based on the characterization results, we proposed a possible conversion mechanism of carbon coating to the inorganic-rich CEI layer. The amorphous carbon network provides good electrical conductivity and allows the transfer of Li^+. The heteroatoms are converted to inorganic Li compounds, while the carbon matrix structure is partially maintained, which restricts side reactions between the cathode and liquid electrolyte and ensures uniform Li^+ flux on the cathode. The dense CEI layer likely promotes electron and ion transfer as the mixed-conductive layer (Figure S37, Supporting Information). The formation of LiF was also confirmed by XRD analysis (Figure 4g,h). The intensity of peaks at 37.5° and 44.8°, corresponding to LiF formation, increased in the F-LFP/C sample during cycling while no obvious signal was in LFP. The results suggest the crystalline LiF formation is favorable when introducing additional F content. The inorganic-rich CEI layer demonstrates superior electrochemical performance to normal CEI composed of organic compounds, Li_2O, LiF, and Li_2CO_3 of low crystallinity.

The effect of carbon coating on the electrical conductivity of LFP was investigated through total density of states (DOS) simulation. Enhanced carrier density was noticed in the LFP structure coated with 0.6 nm amorphous carbon, indicating carbon coating facilitates the electron transfer on LFP surface (Figure S38,

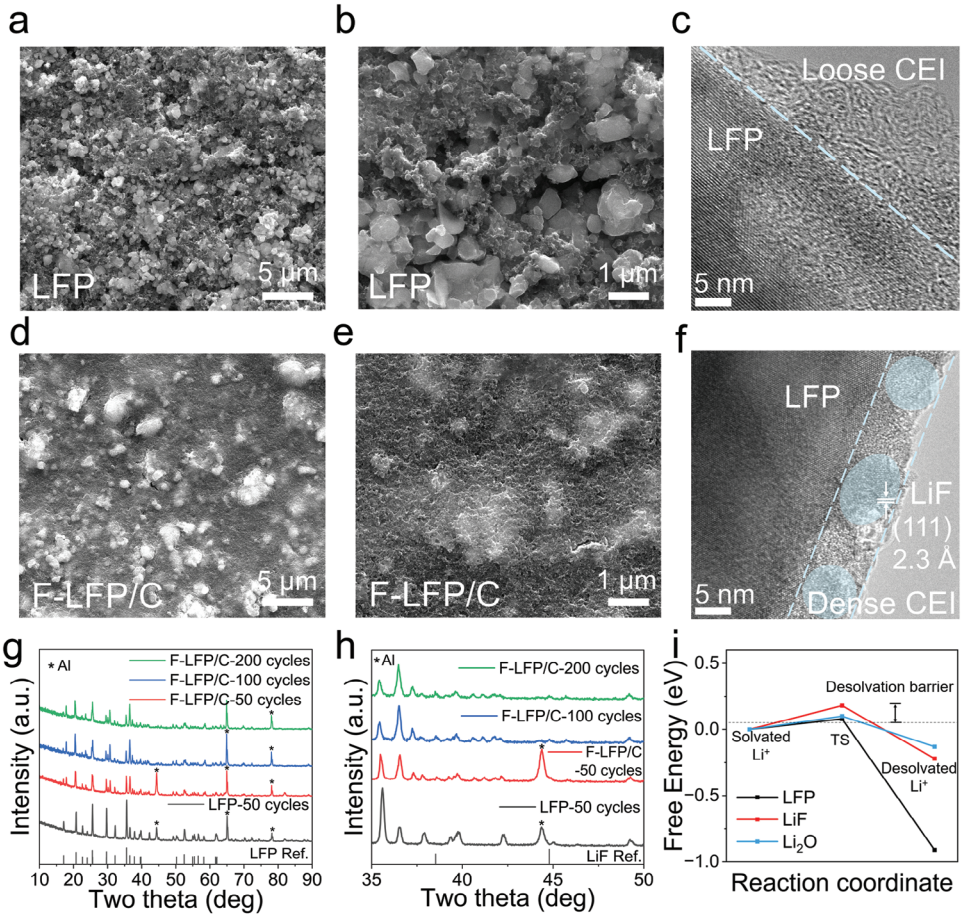

Figure 4. Formation of dense, inorganic-rich cathode-electrolyte interphase. a,b,d,e) SEM images of LFP surfaces and F-LFP/C after testing at 5 C. c,f) HRTEM images of LFP and F-LFP/C surfaces after testing at 5 C. Non-uniform, loose CEI formation was noticed on LFP, while a uniform, dense, crystallized CEI layer formed on the F-LFP/C surface. g,h) XRD patterns of LFP and F-LFP/C samples after cycling at 5 C. Figure h is an expansion of the region from 35° to 50°. The PDF reference cards for each are 00-065-0257 (LFP), 04-012-7777 (LiF) and 00-004-0787 (Al). i) Comparison of energy barriers of different electrode surfaces during Li^+ desolvation process.

Supporting Information). To further investigate the critical factor that determines the effect of heteroatoms, we simulated the Li^+ diffusion and desolvation process in possibly formed inorganic compounds in CEI. The details of the simulation method are shown in Text S2 (Supporting Information). Among various compounds, LiF shows the highest Li^+ diffusion barrier in the lattice (Figure S39, Supporting Information), indicating the ionically insulating character of LiF. The results suggest that the enhanced Li^+ transport property (Figure S33, Supporting Information) in the fluorinated carbon layer is not dominated by the Li^+ diffusion in the inorganic component. The densely packed hybrid CEI layer is important for the fast Li^+ transfer. The step of ionic desolvation, which forms an adsorbed ion at the CEI surface, also plays a crucial role in the Li^+ interfacial transfer from the bulk electrolyte into the host lattice.[56] Due to the high oxygen content of LFP, the Li^+ desolvation is favorable on the LFP surface (Figure S40, Supporting Information) and is not regarded as the rate-determining step in the discharge step. However, we found that the desolvation behavior is affected by the inorganic components on the electrode surface. LiF and Li_2O surfaces showed a similar activation barrier in the desolvation process compared to LFP (Figure 4i; Figure S41 and S42, Supporting Information). Li_3N and Li_3P are less stable during the discharge process due to the high Li concentration on the surface. Li-ions diffuse into the carbonate electrolyte and reduce the organic molecules (Figure S43, Supporting Information). Another factor to be considered is the release of lattice oxygen and interfacial side reactions, which degrades the stability of the cathode materials. A dense CEI layer containing LiF has been reported to suppress the side reactions between electrolyte and electrode, restrict oxygen evolution, and transition metal dissolution.[57,58] Although understanding CEI formation mechanisms and kinetic effects remains challenging, our method provides a convenient way to chemically modify the composition of the CEI, thereby permitting the study of structural changes in performance.

2.5. Life Cycle Assessment (LCA) and Techno-Economic Analysis of Ex Situ Carbon Coating Process

A comparative LCA was conducted to contrast the environmental impact and energy demand of the FJH carbon coating process

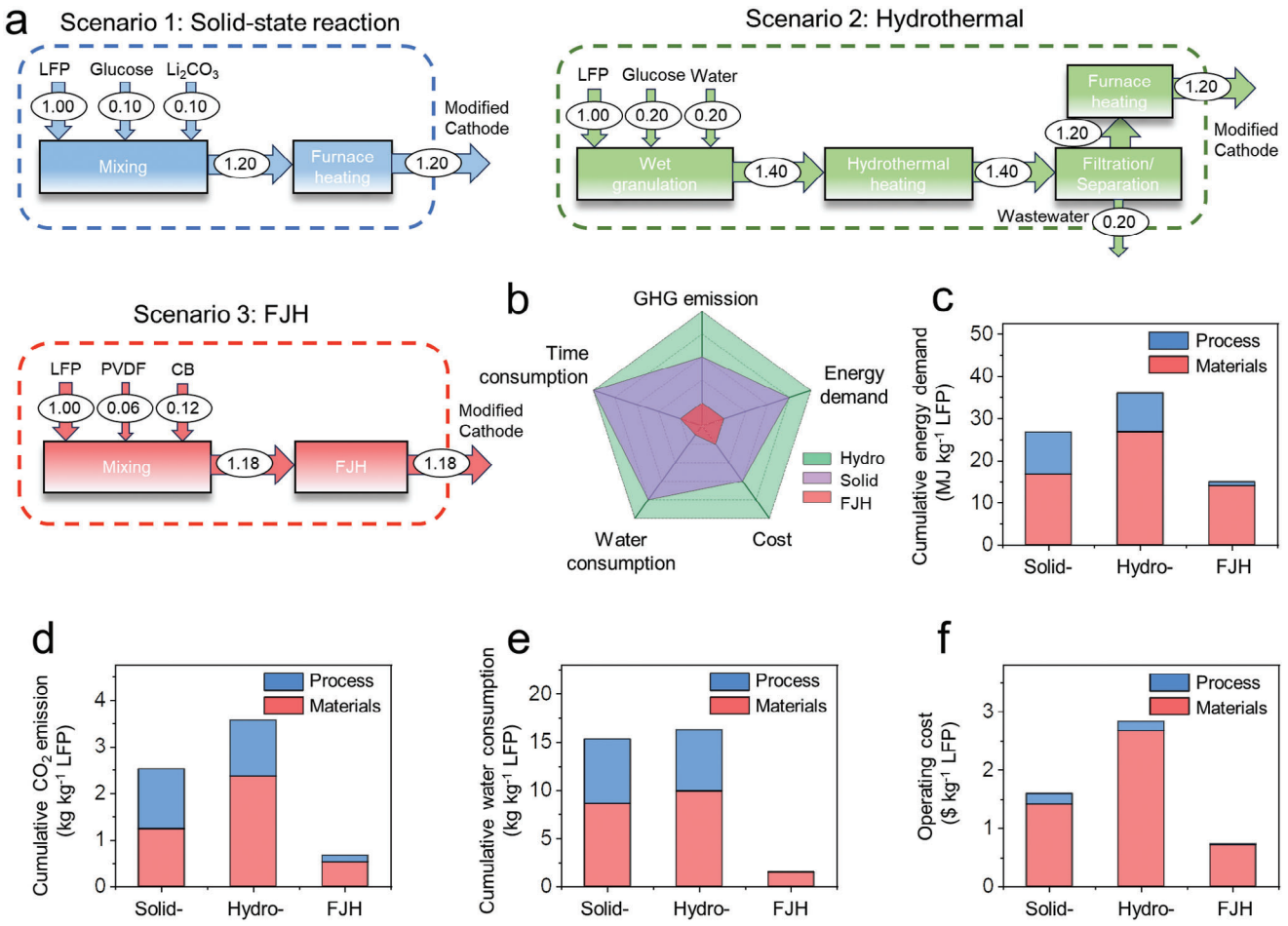

Figure 5. LCA for the ex situ carbon coating process. a) Materials flow analysis of the solid-state, hydrothermal, and FJH processes. b) Comprehensive comparisons of the three scenarios. c) Comparison of cumulative energy demand. d) Comparison of cumulative GHG emissions. e) Techno-economic comparison. The mass flow is normalized to 1 kg of LFP during the carbon coating process.

with other ex situ carbon coating routes, as listed in Text S3 and S4 and Tables S2–S8 (Supporting Information). Three scenarios were considered in this study (**Figure** 5a), including solid-state reaction (LFP was mixed and calcined with a lithium source and carbon source), hydrothermal method (LFP was mixed with a carbon source in water and annealed, then calcined in a furnace), FJH process (LFP was mixed and with a lithium source and carbon source and subjected to FJH).

Three sets of environmental impacts, energy demands, GHG emissions, and water consumption, were analyzed. Benefitting from short reaction time and high energy efficiency, the FJH process significantly decreases five studied categories in the analysis (Figure 5b). Specifically, the FJH process shows a low process energy demand (blue bars in Figure 5c) of 1047 MJ tonne^{-1}, which are ≈90% and 89% lower than that of the solid-state reaction and hydrothermal processes, respectively (Figure 5c; Table S4, Supporting Information). FJH demonstrates a cumulative GHG emission of 136 kg tonne^{-1}, which is much lower than the solid-state reaction (1290 kg tonne^{-1}) and hydrothermal method (1199 kg tonne^{-1}) (Figure 5d; Table S5, Supporting Information). FJH also shows minimal cumulative water use, whereas solid-state and hydrothermal processes require substantial amounts of water (Figure 5e; Table S6, Supporting Information). When synthesizing 1 tonne of carbon-coated LFP, the cost for FJH is as low as $740 tonne^{-1}, including the materials and the process cost, which is 54% and 74% lower than solid-state and hydrothermal processes, respectively (Figure 5f; Tables S7 and S8, Supporting Information). The FJH process has been scaled to 1 tonne per day production rate for the synthesis of graphene,[59] so the likelihood of this process being scalable is encouraging.

3. Conclusion

We developed an ex situ carbon coating method enabled by a rapid and energy-efficient FJH process. By controlling the decomposition of carbon sources and deposition of gas species in a confined reaction chamber, a carbon coating of ≈10 nm thickness can be uniformly achieved on LFP cathodes in 10 s. LFP cathodes with F-doped carbon coating exhibited the highest capacity of 151 mAh g^{-1} at 0.2 C and 96 mAh g^{-1} at 10 C. The heteroatoms from the precursors are enriched on the surface and further converted to inorganic compounds in CEI after battery cycling. The inorganic-rich, compact CEI layer effectively promotes electron and ion transport and restricts the side reactions. Hence,

this facile, low-cost strategy provides a new route for the practical ex situ carbon coating on LFP for LIBs with higher energy density and improved cycling stability. Finally, this FJH method can be applied to other substrates and cathode materials as a post-treatment, offering an ideal platform for electrode-electrolyte interphase engineering and investigation.

4. Experimental Section

Materials: $LiFePO_4$ powder was purchased from MTI Corporation. Carbon black (CB, APS 10 nm, Black Pearls 2000) was purchased from Cabot Corporation. Metallurgical coke was received from SunCoke Energy. Quartz tubing (inner diameter of 8 mm, length of 5 cm) was used for the reaction vessel (500 mg per batch). Polyvinylidene fluoride binder (PVDF, MTI Corporation), boric acid (99.5 wt%, Millipore–Sigma), melamine (99 wt%, Millipore–Sigma), polyethylene glycol (average molecular weight ≈8000, Millipore–Sigma), triphenylphosphine (99 wt%, Millipore–Sigma), and polyphenylene sulfide (average molecular weight ≈10 000, Millipore–Sigma) were used as the precursors in the FJH process. 1-Methyl-2-pyrrolidinone (NMP, 99.5 wt%, Millipore–Sigma) and polyvinylidene fluoride binder (PVDF, MTI Corporation) were used to prepare the battery slurry. The electrolyte was 1 M $LiPF_6$ (battery grade, Millipore–Sigma) mixed with ethylene carbonate (EC) and dimethyl carbonate (DMC) (volume ratio of 3:7). Lithium chips (D = 16 mm, t = 0.6 mm, 99.9 wt%, MTI Corporation) served as the counter electrode in the half cell. Graphite (99.7%, MTI Corporation) was used as the anode in the full cell.

Carbon Coating Process by FJH: Heteroatoms doped carbon-coated LFP powder was synthesized using the flash Joule heating method. LFP, carbon black, and carbon sources are mixed at 85: 10: 5 by weight and ground by mortar and pestle for 0.5 h. The mixture was loaded into a quartz tube (500 mg per batch) with an inner diameter of 8 mm and outer diameter of 12 mm. 200 mg metallurgical coke (12–20 mesh) was mixed with the 500 mg sample above to increase the conductivity during FJH and sieved out after the process. Then, the tube was loaded on a homemade reaction jig and connected to the external flash power system. Graphite rods were used as the electrodes on both sides of the quartz tube and copper wool was used between the graphite rods and the copper electrodes (Figure S1, Supporting Information). The tube was sealed by two O-rings to reduce gas leakage. The resistance can be adjusted by rotating the knob of the FJH reaction jig to compress the sample and is controlled to a value of ≈2 Ω. The jig was put into an Ar-filled desiccator to avoid oxidation of the samples (Figure S2, Supporting Information). The capacitor bank (60 mF rated) was first charged by a direct current (DC) supply. The maximal voltage of the bank can reach 400 V. The relay with programmable delay time with millisecond control was applied to control the discharging time. The flash temperature was recorded by an infrared (IR) thermometer (Micro-Epsilon CTM-3SF75H2-C3) in the range of 200–1500 °C with a detection interval of 1 ms. After flashing, the samples rapidly cooled to room temperature. The pulse sequence used above is 500 ms discharge duration for three times. The three pulses were conducted within a 10 s duration.

GC-MS Analysis: After the FJH process, the possible PVDF degradation compounds were extracted using a mixture of methanol, acetone, and toluene (5 mL solution for ≈500 mg sample). Then the extractant was studied by GC-MS. The injector and the transfer line temperature were set to 120 and 200 °C, respectively. The temperature program was initiated at 48 °C for 3 min, and increased to 80 °C at 8 °C min^{-1}. The carrier gas was helium at a flow rate of 0.5 mL min^{-1}. Manual injection was used to introduce samples. The instrument was an Agilent 8890 GC equipped with an Agilent HP-5 ms low-bleed column (30 m, 0.25 mm internal diameter, 0.25 µm film) and using He carrier gas for liquid and headspace sampling. A tandem Agilent 5977B mass selective detector was used for liquid and headspace gas analysis.

Electrochemical Performance Measurements: To test the electrochemical performance of LFP, the powder was mixed with CB and PVDF at a mass ratio of 85:10:5 in NMP. For the carbon-coated LFP powder containing 10% CB after the FJH process, the powder was mixed with PVDF at a mass ratio of 95:5 in NMP. The slurry was coated on carbon-coated Al foil (≈7 mg cm^{-2} active mass loading with a diameter of 14 mm) and dried in the oven overnight. For the full cell, the F-graphite was obtained by treating commercial graphite using the same FJH conditions to introduce fluorine content on its surface. The F-graphite powder was coated on Cu foil at the mass ratio of 90: 5: 5 to carbon black and PVDF in NMP. The 2032-type coin cell was assembled by employing Li metal foil as anode and LFP as cathode inside an Ar-filled glovebox (O_2 content <0.5 ppm, H_2O content <0.5 ppm). 50 µL 1.0 M $LiPF_6$ electrolyte (in EC: DMC = 3:7 by volume) and Al_2O_3-coated polypropylene were used as the electrolyte and separator, respectively. The coin cells were charged and discharged on a battery working station (LANHE corporation, China) in the air at 25 °C. The test range of the LFP cathode is 2.8 – 3.8 V versus Li/Li^+. After the initial three formation cycles at 0.1 C, the battery was tested at 0.2, 0.5, 1, 2, 5, and 10 C for rate performance. The constant current (CC) mode was used for the test. The stability of the battery cells was tested at 0.5 C and 5.0 C.

Cyclic voltammetry (CV) voltammograms were conducted in the range of 2.8–3.8 V using a CHI 680D electrochemical workstation using different scan rates. Electrochemical impedance spectroscopy (EIS) measurements were performed on the CHI 680D electrochemical workstation by applying an alternating voltage of 5 mV over a frequency ranging from 0.01 Hz to 2 MHz. The active mass loading in each coin cell was ≈7 mg cm^{-2} and the cell was allowed to rest for 12 h before conducting the EIS measurements. The full cell was fabricated using an F-graphite as the anode and F-LFP/C as the cathode. The capacity ratio of F-graphite to F-LFP/C is ≈1.1.

Characterizations: XRD was performed by the Rigaku SmartLab system with a filtered Cu Kα radiation (λ = 1.5406 Å). The FT-IR spectra were obtained by a Thermo Scientific Nicolet 6700 attenuated total reflectance Fourier transform infrared (ATR-FTIR) spectrometer (Waltham, MA, USA). XPS spectra were taken by the PHI Quantera XPS system under a pressure of 5×10^{-9} Torr. The survey spectra were collected with a step size of 0.5 eV and a pass energy of 140 eV, and elemental spectra were collected with a step size of 0.1 eV and a pass energy of 26 eV. All XPS spectra were calibrated using the C 1s peak at 284.8 eV as the reference. The heteroatom ratios are calculated based on its relative ratio to C, O, P, and Fe. The SEM images and element analysis by EDS were taken on the FEI Quanta 400 ESEM FEG system at a voltage of 20 kV and a working distance of 10 mm. TGA was conducted on the Mettler Toledo TGA/DSC 3+ system at a heating rate of 10 °C min^{-1} under 100 mL·min^{-1} air flow or N_2 flow. The HRTEM images were obtained on a JEOL 2100 field emission gun transmission electron microscope at 200 kV. BET measurements were performed on a Quantachrome Autosorb-iQ3-MP/Kr BET surface analyzer at 77 K, where N_2 was used as the adsorption/desorption gas. HAADF-STEM imaging and EDS mapping were carried out on an FEI Titan Themis S/TEM system equipped with image and probe aberration corrections and an electron monochromator operating at 300 kV. The Cu/lacey carbon TEM grid (Ted Pella) was prepared by drop-casting 300 µL of aliquot (1 mg of sample/1 mL ethanol).

Supporting Information

Supporting Information is available from the Wiley Online Library or from the author.

Acknowledgements

The authors thank Dr. Bo Chen of Rice University for the helpful discussion on the XPS results. The funding for the research is provided by the Air Force Office of Scientific Research (FA9550-22-1-0526). C.H.C. and Y.H. acknowledge support from the Welch Foundation (C-2065) and the American Chemical Society Petroleum Research Fund (67236-DNI10). Y.C. is a Rice Academy Fellow (Rice University). Computer resources were provided through DOE's NERSC award BES-ERCAP0027822. The authors also acknowledge the use of the Electron Microscopy Center (EMC) at Rice University. The characterization equipment used in this project is from the Shared Equipment Authority (SEA) at Rice University.

Conflict of Interest

Rice University owns intellectual property on the method described here, but that property is presently unlicensed.

Author Contributions

J.C., O.E.O., Y.C. contributed equally to this work. J.C. and O.O. conceived the idea and designed the experiments. J.C. conducted most characterizations with the help of O.O., Y.C., W.C., and S.X. K.J.S. helped with the GC-MS tests. C.H.C. conducted the HAADF-STEM tests. Y.H. supervised C.H.C. in HAADF-STEM imaging. J.C., O.O., and Y.C. conducted the assembly and electrochemical tests of the LIBs. Y.Z. and B.I.Y. conducted the MD and DFT simulation. J.C. analyzed the simulation results with the assistance of Y.C. Y.C. conducted the LCA and techno-economic analysis. L.E. maintained the flash system and assisted with the reaction temperature measurement. J.C., O.O., Y.C., and J.M.T. wrote and edited the manuscript. All aspects of the research were overseen by J.M.T. All authors discussed the results and commented on the manuscript.

Data Availability Statement

The data that support the findings of this study are available in the supplementary material of this article.

Keywords

carbon coating, cathode-electrolyte interphase, fast charging, Li-ion batteries, Lithium iron phosphate

Received: May 9, 2024
Revised: July 31, 2024
Published online:

[1] R. Schmuch, R. Wagner, G. Hörpel, T. Placke, M. Winter, *Nat. Energy* **2018**, *3*, 267.
[2] B. Namkoong, N. Y. Park, G. T. Park, J. Y. Shin, T. Beierling, C. S. Yoon, Y. K. Sun, *Adv. Energy Mater.* **2022**, *12*, 2200615.
[3] H. H. H Ryu, H. Sun, S.-T., S. Myung, C. Yoon, Y. K. Sun, *Energy Environ. Sci.* **2021**, *14*, 844.
[4] H. Wang, K. Feng, P. Wang, Y. Yang, L. Sun, F. Yang, W. Q. Chen, Y. Zhang, J. Li, *Nat. Commun.* **2023**, *14*, 1246.
[5] S. M. Zhang, J. X. Zhang, S. J. Xu, X. J. Yuan, B. C. He, *Electrochim. Acta* **2013**, *88*, 287.
[6] K. Zaghib, P. Charest, M. Dontigny, A. Guerfi, M. Lagacé, A. Mauger, M. Kopec, C. M. Julien, *J. Power Sources* **2010**, *195*, 8280.
[7] I. D. Johnson, E. Blagovidova, P. A. Dingwall, D. J. L. Brett, P. R. Shearing, J. A. Darr, *J. Power Sources* **2016**, *326*, 476.
[8] C. Y. Chiang, H. C. Su, P. J. Wu, H. J. Liu, C. W. Hu, N. Sharma, V. K. Peterson, H. W. Hsieh, Y. F. Lin, W. C. Chou, C. H. Lee, J. F. Lee, B. Y. Shew, *J. Phys. Chem. C* **2012**, *116*, 24424.
[9] X. Cui, D. Yi, N. Li, L. Zhang, X. Zhang, D. Yang, *Energ. Fuel.* **2020**, *34*, 7600.
[10] D. The Nguyen, J. Kim, Y. Lee, *Chem. Eng. J.* **2023**, *461*, 141750.
[11] M. M. Ren, Z. Zhou, X. P. Gao, W. X. Peng, J. P. Wei, *J. Phys. Chem. C* **2008**, *112*, 5689.
[12] J. Gim, J. Song, D. Nguyen, M. Hilmy Alfaruqi, S. Kim, J. Kang, A. K. Rai, V. Mathew, J. Kim, *Ceram. Int.* **2014**, *40*, 1561.
[13] Q. Hu, J. Y. Liao, B. K. Zou, M. F. Yu, Z. F. Tang, Z. Y. Wen, C. H. Chen, *J. Solid State Electr.* **2018**, *22*, 797.
[14] J. Li, L. Zhang, L. Zhang, W. Hao, H. Wang, Q. Qu, H. Zheng, *J. Power Sources* **2014**, *249*, 311.
[15] L. Sun, Q. Deng, B. Fang, Y. Li, L. Deng, B. Yang, X. Ren, P. Zhang, *CrystEngComm* **2016**, *18*, 7537.
[16] E. Golestani, M. Javanbakht, H. Ghafarian-Zahmatkesh, H. Beydaghi, M. Ghaemi, *Electrochim. Acta* **2018**, *259*, 903.
[17] J. F. Ni, H. H. Zhou, J. T. Chen, X. X. Zhang, *Mater. Lett.* **2007**, *61*, 1260.
[18] D. Bhuvaneswari, N. Kalaiselvi, *Phys. Chem. Chem. Phys.* **2014**, *16*, 1469.
[19] Z. X. Chi, W. Zhang, F. Q. Cheng, J. T. Chen, A. M. Cao, L. J. Wan, *RSC Adv.* **2014**, *4*, 7795.
[20] P. Muzhikara Pratheeksha, E. Hari Mohan, B. Venkata Sarada, M. Ramakrishna, K. Hembram, P. V. V. Srinivas, P. J. Daniel, T. N. Rao, S. Anandan, *Phys. Chem. Chem. Phys.* **2017**, *19*, 175.
[21] Y. Yao, Z. Huang, P. Xie, S. D. Lacey, R. J. Jacob, H. Xie, F. Chen, A. Nie, T. Pu, M. Rehwoldt, D. Yu, M. R. Zachariah, C. Wang, R. Shahbazian-Yassar, J. Li, L. Hu, *Science* **2018**, *359*, 1489.
[22] S. Liu, Y. Shen, Y. Zhang, B. Cui, S. Xi, J. Zhang, L. Xu, S. Zhu, Y. Chen, Y. Deng, W. Hu, *Adv. Mater.* **2022**, *34*, 2106973.
[23] Y. Cheng, J. Chen, B. Deng, W. Chen, K. J. Silva, L. Eddy, G. Wu, Y. Chen, B. Li, C. Kittrell, S. Xu, T. Si, A. A. Martí, B. I. Yakobson, Y. Zhao, J. M. Tour, *Nat. Sustain.* **2024**, *7*, 452.
[24] W. Chen, Y. Cheng, J. Chen, K. V. Bets, R. V. Salvatierra, C. Ge, J. T. Li, D. X. Luong, C. Kittrell, Z. Wang, E. A. McHugh, G. Gao, B. Deng, Y. Han, B. I. Yakobson, J. M. Tour, *Nat. Commun.* **2024**, *15*, 1.
[25] H. Xie, V. K. Champagne III, W. Zhong, B. Clifford, S. Liu, L. Hu, J. C. Zhao, D. R. Clarke, *Adv. Funct. Mater.* **2024**, *34*, 2309978.
[26] R. Saroha, A. K. Panwar, *J. Phys. D: Appl. Phys.* **2017**, *50*, 255501.
[27] S. A. Sarbarze, M. Latifi, P. Sauriol, J. Chaouki, *Can. J. Chem. Eng.* **2019**, *97*, 2259.
[28] K. M. Wyss, J. T. Li, P. A. Advincula, K. V. Bets, W. Chen, L. Eddy, K. J. Silva, J. L. Beckham, J. Chen, W. Meng, B. Deng, S. Nagarajaiah, B. I. Yakobson, J. M. Tour, *Adv. Mater.* **2023**, *35*, 2209621.
[29] B. C. Yu, Y. Hwa, J. H. Kim, H. J. Sohn, *Electrochem. Commun.* **2014**, *46*, 144.
[30] Y. Chen, N. Liu, Y. Jie, F. Hu, Y. Li, B. P. Wilson, Y. Xi, Y. Lai, S. Yang, *ACS Sustainable Chem. Eng.* **2019**, *7*, 18228.
[31] Y. Ji, C. T. Jafvert, N. N. Zyaykina, F. Zhao, *J. Clean. Prod.* **2022**, *367*, 133112.
[32] X. Yuan, K. Luo, Y. Wu, J. He, Z. Zhao, D. Yu, *Nanomaterials* **2018**, *8*, 172.
[33] Q. Huang, K. Wei, H. Xia, *J. Therm. Anal. Calorim.* **2019**, *138*, 3897.
[34] K. M. Wyss, K. J. Silva, K. V. Bets, W. A. Algozeeb, C. Kittrell, C. H. Teng, C. H. Choi, W. Chen, J. L. Beckham, B. I. Yakobson, J. M. Tour, *Adv. Mater.* **2023**, *35*, 2306763.
[35] Y. Kitahara, S. Takahashi, T. Fujii, *Chemosphere* **2012**, *88*, 663.
[36] L. H. Perng, *Polym. Degrad. Stab.* **2000**, *69*, 323.
[37] J. Wang, X. Sun, *Energy Environ. Sci.* **2012**, *5*, 5163.
[38] X. Cai, T. Lei, D. Sun, L. Lin, *RSC Adv.* **2017**, *7*, 15382.
[39] L. Kong, Y. Li, W. Feng, *Trans. Tianjin Univ.* **2022**, *28*, 123.
[40] P. Viswanath, M. Yoshimura, *SN Appl. Sci.* **2019**, *1*, 1519.
[41] Z. Yan, D. Huang, X. Fan, F. Zheng, Q. Pan, Z. Ma, H. Wang, Y. Huang, Q. Li, *Front. Mater. Sci.* **2020**, *6*, 341
[42] T. T. Wei, X. Liu, S. J. Yang, P. F. Wang, T. F. Yi, *J. Energy Chem.* **2023**, *80*, 603.
[43] H. Chang, L. Zhao, S. Zhao, Z. L. Liu, P. F. Wang, Y. Xie, T. F. Yi, *J. Energy Chem.* **2024**, *93*, 400.
[44] H. Bluhm, *Woodhead Publishing Series in Electronic and Optical Materials* **2011**, 75.
[45] N. O. Laschuk, E. B. Easton, O. V. Zenkina, *RSC Adv.* **2021**, *11*, 27925.
[46] T. T. Wei, P. Peng, Y. R. Ji, Y. R. Zhu, T. F. Yi, Y. Xie, *J. Energy Chem.* **2022**, *71*, 400.

[47] K. Jia, J. Ma, J. Wang, Z. Liang, G. Ji, Z. Piao, R. Gao, Y. Zhu, Z. Zhuang, G. Zhou, H. M. Cheng, *Adv. Mater.* **2023**, *35*, 2208034.
[48] B. Zhang, Y. Xu, J. Wang, X. Ma, W. Hou, X. Xue, *Electrochim. Acta* **2021**, *368*, 137575.
[49] Sungjemmenla, S. K. Vineeth, C. B. Soni, V. Kumar, Z. W. Seh, *Energy Technol.* **2022**, *10*, 2200421.
[50] P. Bai, X. Ji, J. Zhang, W. Zhang, S. Hou, H. Su, M. Li, T. Deng, L. Cao, S. Liu, X. He, Y. Xu, C. Wang, *Angew. Chem., Int. Ed.* **2022**, *61*, e202202731.
[51] Y. Qian, P. Niehoff, M. Börner, M. Grützke, X. Mönnighoff, P. Behrends, S. Nowak, M. Winter, F. M. Schappacher, *J. Power Sources* **2016**, *329*, 31.
[52] Z. Feng, R. Rajagopalan, D. Sun, Y. Tang, H. Wang, *Chem. Eng. J.* **2020**, *382*, 122959.
[53] Z. Zhu, Y. Liang, H. Hu, A. Gao, T. Meng, D. Shu, F. Yi, J. Ling, *J. Power Sources* **2021**, *498*, 229857.
[54] Z. Zhang, J. Yang, W. Huang, H. Wang, W. Zhou, Y. Li, Y. Li, J. Xu, W. Huang, W. Chiu, Y. Cui, *Matter* **2021**, *4*, 302.
[55] S. Zhou, X. Zhang, Z. Zhang, S. Liu, R. Wang, *Coatings* **2023**, *13*, 727.
[56] P. M. Chekushkin, I. S. Merenkov, V. S. Smirnov, S. A. Kislenko, V. A. Nikitina, *Electrochim. Acta* **2021**, *372*, 137843.
[57] S. P. Kühn, K. Edström, M. Winter, I. Cekic-Laskovic, *Adv. Mater. Interfaces* **2022**, *9*, 2102078.
[58] L. Di, C. Yufang, S. Weiwei, X. Wei, Y. Shuaiyu, L. Shiqiang, Z. Lanlan, Z. Yanshuang, Y. Tianyan, X. Peitao, Z. Chunman, *Adv. Energy Mater.* **2023**, *13*, 2301765.
[59] Universal Matter, https://www.universalmatter.com/ (accessed: July 2024).